Asociación Argentina
de Mecánica Computacional

Mecánica Computacional Vol XXVII, págs. 541-561 (artículo completo)
Alberto Cardona, Mario Storti, Carlos Zuppa. (Eds.)
San Luis, Argentina, 10-13 Noviembre 2008

APPLICATIONS OF THE IMMERSED ELEMENT-FREE GALERKIN METHOD

Claudio M. Pita[a], Sergio D. Felicelli[b]

[a] *Department of Mechanical Engineering, Mississippi State University, MS 39762, USA, cmp220@msstate.edu, http://msstate.me.edu*
[b] *Department of Mechanical Engineering, Mississippi State University, MS 39762, USA, felicelli@me.msstate.edu, http://msstate.me.edu*

Keywords: Meshfree, Solid-fluid interaction, Element-free Galerkin, Moving Least Squares.

Abstract. In this paper, we present a new numerical method, the Immersed Element-Free Galerkin Method (IEFGM), for the solution of fluid-structure interaction problems. The technique is a variation of the Immersed Finite Element Method developed by (L. Zhang et al., *Journal of Fluids and Structures*, 23(6):836-857 (2007)) in which the fluid-solid interaction force is represented as a volumetric force in the momentum equations. In IEFGM, a Lagrangian solid domain moves on top of an Eulerian fluid domain which spans over the entire computational region. In this work, the fluid (Eulerian) domain is modeled using the finite element method and the solid (Lagrangian) domain is modeled using the element-free Galerkin method. We assure the continuity between the solid and fluid domains by means of a local approximation, in the vicinity of the solid domain, of the velocity field and the fluid-structure interaction force. Such an approximation is achieved using the moving least squares (MLS) technique. The method is applied to simulating the motion of rigid and deformable objects falling in a viscous fluid. Good performance of the method is obtained when comparing simulated results with analytical solutions or published works using other numerical approaches. The method is currently being enhanced to simulate the transport of deformable inclusions in liquid metals.

1 INTRODUCTION

Numerical investigations involving large deformation type problems require reliable numerical modeling and simulation techniques. According to Li and Liu (2004), the FEM subdivision procedure is not always advantageous in computations involving large deformations. For more than 30 years, many research efforts have been devoted to adapt the FEM subdivision to topological and geometrical changes in the domain of interest, occurring, for instance, during the deformation of the material. The so-called Arbitrary Lagrangian Eulerian (ALE) method is a finite element formulation that moves the mesh independently from the material motion, allowing mesh distortion to be minimized. But even this technique has its limitations for some practical problems such as fluid flow or large strain continuum deformation.

With the aim of finding a better approximation of continuum compatibility, a series of new discretization methods, called Meshfree Particle Methods, were developed, Belytschko et al. (1994), Li and Liu (2004) and Liu (2003). Meshfree particle methods have been designed to improve the inadequacy of FEM discretization. The main idea of these innovative methods is to discretize a continuum by only a set of nodal points without additional mesh constraints. The meshfree methods have a clear advantage over the traditional finite element methods because meshfree interpolants have a larger support size than FEM interpolants. Smoothed Particle Hydrodynamics is one of the earliest particle methods in computational mechanics. In 1977, Gingold et al. (1977) and Lucy (1977) initially developed the SPH method for the simulation of astrophysics problems. Their breakthrough was a method for the calculation of derivatives that did not require a structured computational mesh. Review papers by Benz (1990) and Monaghan (1982) cover the early development of SPH. Libersky and Petchek (1990) extended SPH to work with the full stress tensor in 2D. This addition allowed SPH to be used in problems where material strength is important. The development of SPH with strength of materials continued with extension to 3D by Libersky et al. (1993), and the linking of SPH with existing finite element codes by Attaway et al. (1994) and Johnson (1994). The introduction of material strength highlighted shortcomings in the basic method: accuracy, tensile instability, zero energy modes and artificial viscosity. These shortcomings were identified in the first comprehensive analysis of the SPH method by Swegle et al. (1994) and Wen et al. (1994). The problems of consistency and accuracy of the SPH method, identified by Belytschko et al. (1996), were addressed by Randles et al. (1996) and Vignjevic et al. (2000). This resulted in a normalized first order consistent version of the SPH method with improved accuracy. The attempts to ensure first order consistency in SPH led to the development of a number of variants of the SPH method, such as Element Free Galerkin Method (EFGM) by Belytschko et al. (1994) and Krongauz et al. (1997), Reproducing Kernel Particle Method (RKPM) by Liu et al. (1993, 1995), Moving Least Square Particle Hydrodynamics (MLSPH) by Dilts (1999), and the Meshless Local Petrov Galerkin Method (MLPG) by Atluri et al. (2000). These methods allow the restoration of consistency of any order by means of a correction function. It has been shown in Atluri et al. (2000) that the approximations based on corrected kernels, like RKPM, are equivalent to moving least square approximations, like EFGM. The issue of stability was dealt with in the context of particle methods in general by Belytschko et al. (2002), and independently by Randles et al. (1999). They reached the same conclusions as Swegle et al. (1994) in his initial study.

The RKPM approximation functions have been used by Zhang et al. (2004) and Zhang et al. (2007) to develop the immersed finite element method (IFEM) to model fluid-solid interaction processes. In this method, a Lagrangian solid mesh moves on top of a background

Eulerian fluid mesh which spans over the entire computational domain. The fluid-structure interaction is represented as a body force term in the momentum equations. Although the IFEM uses the mesh-free RKPM interpolants to couple the solid and fluid domains, a finite element discretization is used for both regions. An improvement of the IFEM with respect to the previously developed immersed boundary method is that the structural models in IFEM are not restricted to one-dimensional volumeless structures such as fibers; instead they may occupy a finite volume in the fluid and a constitutive model can be used to calculate the deformation and stress in the solid

The aim of the present work is to extend the ideas of the IFEM to develop a new technique, the Immersed Element-Free Galerkin Method, suitable for handling a larger set of fluid-structure interaction problems. In our approach, the fluid domain is modeled using an Eulerian formulation with the finite element method (similarly as IFEM), however, we use a meshfree particle method (the EFGM) to model the solid domain. In addition, the coupling between the solid and fluid domains is achieved by means of a Moving Least Squares local approximation of the fluid velocity field and the interaction force in the vicinity of the solid region. This approach makes the new method an attractive technique for the simulation of FSI problems with highly deformable solids.

NOMENCLATURE

Ω : Computational domain.
Ω^f : Fluid domain.
Ω^s : Solid domain.
$\bar{\Omega}$: Overlapping domain.
$\boldsymbol{x}^s$: Solid particles current position.
$\boldsymbol{x}$: Fluid particles current position.
$f_i^{FSI,s}$: i-th Cartesian component of the fluid-solid interaction force in the solid domain.
f_i^{FSI} : i-th Cartesian component of the fluid-solid interaction force in the fluid domain.
v_i^s : i-th Cartesian component of the solid particles velocity.
v_i : i-th Cartesian component of the fluid nodes velocity.
ρ^s : Density of solid.
ρ^f : Density of fluid.
σ_{ij}^s : Cauchy stress tensor for the solid.
σ_{ij}^f : Cauchy stress tensor for the fluid.
g_i : i-th Cartesian component of the acceleration of gravity.
np : Number of nodes in the fluid Eulerian grid.
npL : Number of particles in the Lagrangian solid domain.
w : Weight function.
$\boldsymbol{v}^h$: Local Moving Least Squares (MLS) approximation of the fluid velocity field.
$\boldsymbol{\phi}$: MLS shape function.
$x_i^{s,n}$: i-th Cartesian component of the solid particles position at time step n.
E : Young's modulus.
μ : Viscosity of the fluid.
C_D : Drag coefficient.

2 FORMULATION OF THE IMMERSED ELEMENT-FREE GALERKIN METHOD

2.1 Basic definitions

Let us consider a two dimensional deformable solid body, Ω^s, that is completely immersed in a fluid domain, Ω^f. These two domains do not intersect, and their union defines the computational domain Ω. Therefore we can write:

$$\Omega^f \cup \Omega^s = \Omega$$
$$\Omega^f \cap \Omega^s = \emptyset \quad (1)$$

Assuming that the material in both the solid and fluid domains are incompressible and that the no-slip condition between solid and fluid regions applies, the union of the two domains can be treated as one continuum incompressible domain with a continuous velocity field. In this work, the fluid domain is modeled using the finite element method with an Eulerian formulation where the independent variables are the node's time-invariant actual position $\boldsymbol{x}$ and the actual time t, and the dependent variables are the velocity field $\boldsymbol{v}$ and the pressure field p. On the other hand, the solid domain is modeled using the element-free Galekin method with an updated Lagrangian formulation where the independent variables are the particle's position in the current configuration $\boldsymbol{x}^s$ and the actual time t, and the dependent variable is the particle's displacement $\boldsymbol{u}^s$ defined as the difference between the current and previous position. A schematic of the fluid and solid domains including the independent variables of each formulation and the displacement of the solid particles is presented in Fig. 2.1. Note that for clarity we use the notion of node to refer to the fluid domain (described with a finite element method), and the notion of particle to make reference to the solid domain (described with an element-free method).

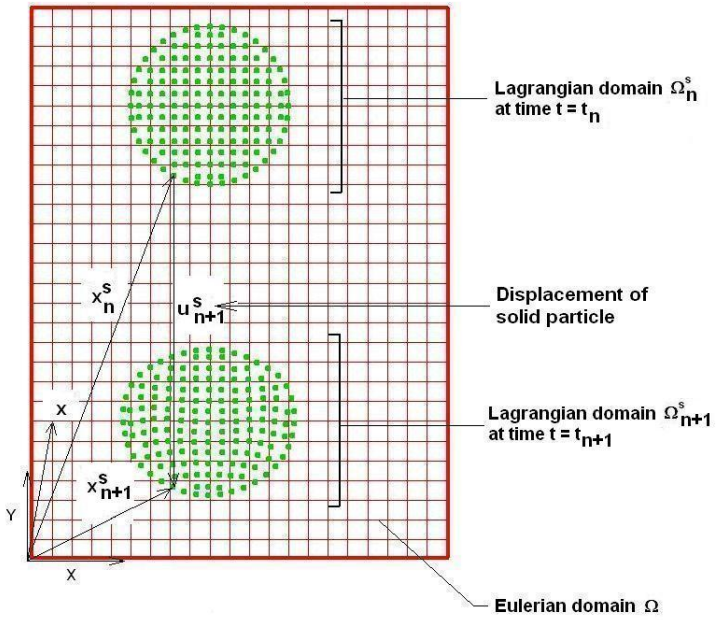

Fig. 2.1: Definition of the solid (Lagrangian) domain and the fluid (Eulerian) domain. The Eulerian configuration is characterized by the time invariant position vector $\boldsymbol{x}$ whereas the Lagrangian configuration is characterized by the current position vector $\boldsymbol{x}^s$.

2.2 Overlapping domain

In the real problem that we want to solve, the geometrical relationships between the solid and fluid domains are given by Eq. 1. Following the approach adopted by Zhang et al. (2007) in their IFEM method, we assume that the fluid domain occupies the entire computational domain, therefore $\Omega=\Omega^f$ and that the solid domain is placed on top of the fluid region. This assumption introduces what is called an overlapping domain ($\bar{\Omega}$). The overlapping domain is the region where the solid and fluid domains coexist (i.e., $\bar{\Omega} = \Omega^s$). Note that this is a simplifying assumption and does not correspond with the real physics of the problem. This assumption simplifies the computations allowing the equations for the fluid and the solid domains to be solved independently. It also allows the independent discretization of the fluid and solid regions. The drawback of these simplifications is that the overlapping domain introduces non-physical effects in the equations of motion that should be carefully considered.

2.3 Strong form of the governing equations

In this section we present the equations of motion for the IEFGM method. The fluid-solid interaction force within the domain Ω^s is denoted as $f_i^{FSI,s}$, where FSI stands for fluid-solid interaction, *s* means that the expression is valid within the solid domain and the sub-index *i* represents the i-th Cartesian component of the force vector field.

$$f_i^{FSI,S} \stackrel{\text{def}}{=} -(\rho^s - \rho^f)\frac{dv^s{}_i}{dt} + \sigma^s_{ij,j} - \sigma^f_{ij,j} + (\rho^s - \rho^f)g_i \quad \forall \boldsymbol{x}^s \in \Omega^s \tag{2}$$

Note that Eq. 2 is simply a force balance in the updated Lagrangian solid domain. The interaction force is treated as an additional body force acting on the solid. Neglecting the fluid stress within the solid domain and recognizing that the total time derivative equals the partial time derivative, we can rewrite Eq. 2 as:

$$f_i^{FSI,S} = -(\rho^s - \rho^f)\frac{\partial v^s{}_i}{\partial t} + \sigma^s_{ij,j} + (\rho^s - \rho^f)g_i \quad \forall \boldsymbol{x}^s \in \Omega^s \tag{3}$$

In Eq. 3, the variables are defined using an updated Lagrangian formalism. This equation represents the strong form of the governing linear momentum equation for the solid domain. In this work we considered the solid to be an elastic material with the stress-strain relationship given by the generalized Hooke's law.

With the concept of fluid-solid interaction force in mind, we can combine the Navier-Stokes equation for the fluid domain (Ω^f) with the interaction force in the overlapping domain ($\bar{\Omega}$) and write, as in Li and Liu (2004), the modified Navier-Stokes equation for the entire Eulerian computational domain (Ω):

$$\rho^f \frac{dv_i}{dt} = \sigma^f_{ij,j} + f_i^{FSI} \quad \forall \boldsymbol{x} \in \Omega \tag{4}$$

In Eq. 4, the external force applied to the fluid domain has been neglected. Note that the only difference between this equation and the Navier-Stokes equation is the last term in the

right hand side, namely f_i^{FSI}. This term accounts for the "extra" artificial fluid contained in the overlapping domain, as mentioned in section 2.1. The two interaction forces f_i^{FSI} and $f_i^{FSI,s}$ constitute an action-reaction force pair. The force f_i^{FSI} acts on the overlapping domain whereas the force $f_i^{FSI,s}$ acts on the solid domain. These two domains are in contact and interact with each other. Moreover, since the discretizations of the two aforementioned regions are not coincident, we need to distribute the force $f_i^{FSI,s}$ (acting on Ω^s) onto the entire Eulerian computational domain (Ω). The way in which we approach this distribution is a central point of this work and it is explained in section 2.5.2.

Since we consider the whole domain Ω to be incompressible, we apply the incompressibility constraint as:

$$v_{i,i} = 0 \quad \forall \boldsymbol{x} \in \Omega \tag{5}$$

Eq. 4 and Eq. 5, with the variables defined using the Eulerian formalism, represent the strong forms of the governing equations for the entire Eulerian computational domain ($\Omega^f \cup \bar{\Omega} = \Omega$).

2.4 Weak form of the governing equations

To derive the weak form of Eq. 3, we multiply it by an arbitrary test function δu_i and integrate over the entire current solid domain.

$$\int_{\Omega^s} \delta u_i f_i^{FSI,s} d\Omega = \int_{\Omega^s} \delta u_i \left[-(\rho^s - \rho^f) \frac{\partial v^s{}_i}{\partial t} + \sigma^s_{ij,j} + (\rho^s - \rho^f) g_i \right] d\Omega \tag{6}$$

After integrating by parts the second term in the right hand side, we obtain:

$$\int_{\Omega^s} \delta u_i f_i^{FSI,s} d\Omega = \int_{\Omega^s} \delta u_i \left[-(\rho^s - \rho^f) \frac{\partial v^s{}_i}{\partial t} + (\rho^s - \rho^f) g_i \right] d\Omega + \int_{\Omega^s} \delta u_{i,j} \sigma^s_{ij} \, d\,\Omega \tag{7}$$

In accordance with Zhang et. al. (2007), the boundary terms in the fluid-structure interface for both fluid and solid governing equations will cancel each other and they are not included in the weak form for clarity. Eq. 7 constitutes the weak form of the linear momentum equation for the Lagrangian solid domain.

In the same fashion we can obtain the weak forms of the governing equations (linear momentum and continuity) for the fluid domain, given by Eq. 4 and Eq. 5, obtaining:

$$\int_{\Omega} \delta v_i \rho^f \frac{dv_i}{dt} d\Omega = \int_{\Omega} \delta v_{i,j} \sigma^f_{ij} d\Omega + \int_{\Omega} \delta v_i f_i^{FSI} d\Omega \tag{8}$$

Remembering that the computational domain is described using an Eulerian formulation, the total time derivative may be expressed as:

$$\frac{dv_i}{dt} = v_{i,t} + v_j v_{i,j} \tag{9}$$

Replacing Eq. 9 into Eq. 8, we obtain:

$$\int_\Omega \delta v_i \rho^f (v_{i,t} + v_j v_{i,j})\, d\Omega = \int_\Omega \delta v_{i,j} \sigma_{ij}^f d\Omega + \int_\Omega \delta v_i f_i^{FSI} d\Omega \qquad (10)$$

Similarly, the weak form of the continuity equation is:

$$\int_\Omega \delta p v_{i,i}\, d\Omega = 0 \qquad (11)$$

Note that in Eq. 10 and Eq. 11, we used two different test functions δvi and δp respectively. These two equations constitute the weak form of the linear momentum and continuity equations for the Eulerian computational domain. In this work, we used a penalty formulation to impose incompressibility in the fluid domain, and a Petrov-Galerkin technique to treat the advection term Felicelli et al. (1993).

2.5 Coupling between the solid and fluid domains

A critical point in the development of a numerical code capable of simulating fluid-solid interaction problems is the coupling between the fluid and solid domains. Two critical variables relevant to this coupling are the solid domain velocity $v^s(\mathbf{x},t)$ and the interaction force acting on the overlapping domain f_i^{FSI}.

2.5.1 Solid domain velocity v^s

As previously mentioned, we consider a no-slip condition between the solid and the fluid domains. Moreover, since the discretizations of the solid and fluid regions are independent, the nodes of the Eulerian mesh in the fluid domain will in general not coincide with the moving particles of the solid domain at every time step. Therefore a coupling between the fluid nodal velocity $\mathbf{v}(\mathbf{x},t)$ and the solid particles velocity $v^s(\mathbf{x},t)$ is needed. The position of the solid particles is then updated based on the calculated velocity field. The coupling between the two velocity fields is accomplished by means of a local approximation of the fluid velocity field.

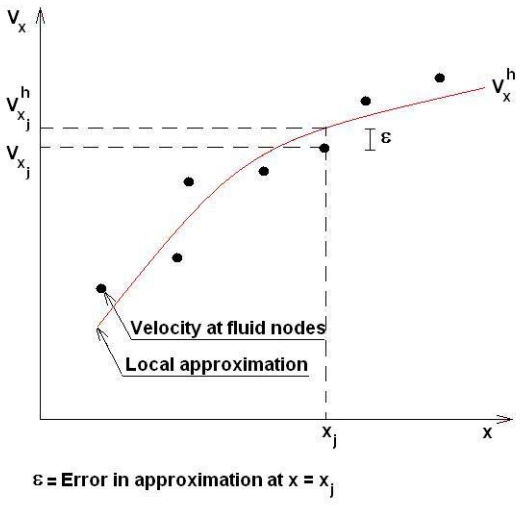

Fig. 2.2: Schematic representation of the local approximation of the x-component of the fluid nodal velocity (v_x). The dots represent the velocity at different nodes in the Eulerian fluid mesh. The solid curve represents the local approximation of the x-component of the fluid velocity field.

In Fig. 2.2 we show a schematic representation of the local approximation of the x-component of the fluid nodal velocity field (v_x). The dots represent the nodal values of the fluid velocity and the solid curve represents the approximated continuum velocity field (v_x^h). The approximation is done by means of the moving least squares (MLS) procedure. Several authors, Levin (1998) and Lancaster et al. (1981), have used the MLS procedure to approximate a set of scattered data.

The main objective of the MLS procedure is to minimize a weighted residual functional J constructed using the approximated nodal values of the fluid velocity field (solid curve in Fig. 2.2 evaluated at nodal positions) and the nodal values of the fluid velocity field calculated with the finite element method (dots in Fig. 2.2). The weighted residual functional is defined as:

$$J \stackrel{\text{def}}{=} \sum_{j=1}^{np} w(\boldsymbol{x}-\boldsymbol{x}_j)\left[v_i^h(\boldsymbol{x}-\boldsymbol{x}_j) - v_i(\boldsymbol{x}_j)\right]^2 \tag{12}$$

In Eq. 12, the sub-index i represents the i-th Cartesian direction and the summation goes over all the Eulerian nodes in the finite element mesh that are included inside the support domain of $\boldsymbol{x}$. We propose an approximated field function of the form:

$$v^h(\boldsymbol{x}) \stackrel{\text{def}}{=} \sum_{j=1}^{m} p_j(\boldsymbol{x})\, a_j(\boldsymbol{x}) = \boldsymbol{p}^T(\boldsymbol{x}).\boldsymbol{a}(\boldsymbol{x}) \tag{13}$$

where m is the number of monomials in the polynomial basis $\boldsymbol{p(x)}$ and $\boldsymbol{a(x)}$ is a vector of unknown coefficients which are functions of $\boldsymbol{x}$. In this work we used a linear 2D basis defined as: $\boldsymbol{p}(\boldsymbol{x}) \stackrel{\text{def}}{=} \{1, x, y\}$.

In the MLS approximation, at an arbitrary point $\boldsymbol{x}$, $\boldsymbol{a(x)}$ is chosen to minimize the weighted residual functional J. Therefore the minimization condition is expressed as:

$$\frac{\partial J}{\partial \boldsymbol{a}} = 0 \tag{14}$$

A detailed description of the minimization process can be found in Belytschko et al. (1994), Liu (2003), Levin (1998), Lancaster et al. (1981), and Dolbow et al. (1998). The final approximated field function may be expressed as:

$$\boldsymbol{v}^h(\boldsymbol{x}) = \sum_j \phi_j(\boldsymbol{x})\boldsymbol{v}(\boldsymbol{x}_j) \qquad \forall \boldsymbol{x}_j \in \Omega_x \tag{15}$$

The MLS shape functions are defined as:

$$\phi_j(\boldsymbol{x}) \stackrel{\text{def}}{=} \boldsymbol{p}^T(\boldsymbol{x}).\left[\sum_{i=1}^{np} w(\boldsymbol{x}-\boldsymbol{x}_i).\boldsymbol{p}(\boldsymbol{x}_i).\boldsymbol{p}^T(\boldsymbol{x}_i)\right]^{-1}.w(\boldsymbol{x}-\boldsymbol{x}_j).\boldsymbol{p}(\boldsymbol{x}_j) \tag{16}$$

In Eq. 15, the fluid velocity at position $\boldsymbol{x}$ can be calculated from the velocities at nodes of the Eulerian mesh within the influence domain Ω_x of the point at position $\boldsymbol{x}$. A detailed explanation of the method used to estimate the influence domain is presented in Liu (2003).

In summary, $\boldsymbol{v}^h\boldsymbol{(x)}$ in Eq. 15 represents the local MLS approximation of the fluid velocity

field. The x-component of $\boldsymbol{v}^h(\boldsymbol{x})$ is what is depicted by the solid curve in Fig. 2.2.

Since we are considering a no-slip condition between the fluid and solid domains, we can write:

$$\boldsymbol{v}^h(\boldsymbol{x}) = \boldsymbol{v}^s(\boldsymbol{x}) \quad \forall \boldsymbol{x} \in \Omega^s \equiv \bar{\Omega} \tag{17}$$

Therefore, by considering points $\boldsymbol{x} \in \Omega^s$ in the solid domain, Eq. 15 can also be used to obtain the solid velocity field $\boldsymbol{v}^s(\boldsymbol{x})$:

$$\boldsymbol{v}^s(\boldsymbol{x}^s) = \sum_j \phi_j(\boldsymbol{x}^s)\boldsymbol{v}(\boldsymbol{x}_j) \quad \forall \boldsymbol{x}_j \in \Omega_x \tag{18}$$

2.5.2 Distribution of the interaction force, f_i^{FSI}, in the fluid domain

Eq. 3 gives the solid-fluid interaction force at each solid particle. To distribute this force onto the fluid nodes we used the same approach as for the velocity field approximation in the solid domain, i.e., the MLS procedure. The local approximation of the interaction force can be expressed as:

$$f_i^{FSI,s}(\boldsymbol{x}^s) = \sum_j \phi_j(\boldsymbol{x}^s) f_i^{FSI,s}(\boldsymbol{x}_j^s) \quad \forall \boldsymbol{x}_j^s \in \Omega_{x^s} \tag{19}$$

In Eq. 19, the interaction force is obtained from the interaction forces at solid particles $\boldsymbol{x}_j^s$ contained in the influence domain Ω_x^s of the solid point located at position $\boldsymbol{x}^s$.

As mentioned in section 2.3, the two interaction forces f_i^{FSI} and $f_i^{FSI,s}$ constitute an action and reaction force pair and, by definition, they must be equal in magnitude and act in opposite directions.

$$f_i^{FSI,s}(\boldsymbol{x}) = -f_i^{FSI}(\boldsymbol{x}) \quad \forall \boldsymbol{x} \in \bar{\Omega} \tag{20}$$

Therefore, by considering points in the Eulerian fluid mesh $\boldsymbol{x}^s = \boldsymbol{x} \in \Omega$, and using Eq. 19, we distribute the interaction force onto the fluid domain obtaining $f_i^{FSI}(\boldsymbol{x})$.

$$f_i^{FSI}(\boldsymbol{x}) = \sum_j \phi_j(\boldsymbol{x}) f_i^{FSI,s}(\boldsymbol{x}_j) \quad \forall \boldsymbol{x}_j \in \Omega_x \tag{21}$$

In Eq. 21, Ω_x represents the influence domain of the point at position $\boldsymbol{x}$ in the fluid region.

2.6 Updating the position of the solid particles

Since we are considering a current Lagrangian description for the solid domain, the position of the solid particles can be updated from the solid velocity calculated in Eq. 18:

$$x_i^{s,n+1} = x_i^{s,n} + v_i^{s,n+1}\Delta t \tag{22}$$

Where the index $n+1$ indicates quantities evaluated at the current time step and Δt is the time step size.

2.7 Algorithm

In this section we summarize the assumptions made for the fluid and the solid domain and the proposed algorithm. The assumptions made are the following:

a. The fluid is incompressible.
b. The solid is incompressible.
c. The solid must remain immersed in the fluid at all times during the simulation.
d. No-slip condition between the solid and fluid domains.

It is important to remember that the variables in the solid domain Ω^s are defined using a current Lagrangian formalism whereas the variables in the fluid domains are defined using an Eulerian formalism.

The algorithm for the IEFGM can be outlined as follows:

a) Set the initial position of all the solid particles at time $t=0$ (Ω_o^s) and assume a non-zero small constant velocity in the overlapping domain.
b) Calculate the fluid-solid interaction force $f_i^{FSI,s}$ at the solid particles using Eq. 7.
c) Distribute the solid-fluid interaction force from the solid domain onto the fluid domain (from $f_i^{FSI,s}$ to f_i^{FSI}) using Eq. 21.
d) Approximate the solid velocity $\boldsymbol{v}^s$ using Eq. 18.
e) Update the positions of the solid particles using Eq. 22.
f) Solve for the fluid velocities and pressure distribution using Eq. 10 and Eq. 11.

2.7.1 Important points

- The fact that the interaction force f_i^{FSI} is added in an explicit manner to the Navier-Stokes equation for the fluid, Eq. 8, restricts the size of the time step to be used. The more rigid the solid material, the smaller the time step needed for convergence.
- According to Zhang et al. (2007), the fluid mesh spacing has to be approximately twice the background solid mesh spacing to avoid fluid sinking through into the solid domain. It is appropriate to maintain the fluid grid larger than the solid background mesh but not too large because it may cause a decrease in accuracy. Note that even though in this work the solid is being modeled using the EFG meshfree method, as detailed in Dolbow et al. (1998), we still need a background mesh in the solid region for integration of the weak-form equations.

3 NUMERICAL EXAMPLES

In this work we studied two two-dimensional numerical examples to explore the capability and performance of the IEFG formulation. The simulated examples are: a rigid disk and a soft disk, both falling in a viscous fluid. For the two cases, we considered the solid to be an incompressible elastic material governed by Hook's constitutive law.

$$\sigma_{xx} = \frac{E}{(1-\nu^2)}(\epsilon_{xx} + \nu\epsilon_{yy})$$

$$\sigma_{yy} = \frac{E}{(1-\nu^2)}(\epsilon_{yy} + \nu\epsilon_{xx})$$

$$\sigma_{xy} = \sigma_{yx} = \frac{E}{(1+\nu)}\epsilon_{xy} \tag{23}$$

The same Eulerian finite element mesh was used to calculate the fluid velocity in the two examples. This consisted of 3321 rectangular bilinear elements occupying a region 10 mm wide by 20 mm high. For the solid-disk geometry we considered 161 particles. In both examples, and at all time steps, the positions of the solid particles were coincident with the positions of the solid nodes of the background-integration mesh.

The fluid and solid geometrical and material properties are summarized in Table1. The properties of the fluid are similar to those of a Pb-Sn liquid metal, with a heavier solid material. Although not presented in this work, we plan to apply the method to simulate the transport of inclusions during solidification of alloys.

	Fluid domain	Solid domain
w (m)	0.01	-
h (m)	0.02	-
d (m)	-	0.002
ρ *(Kg/m³)*	8800.0	12000.0
μ *(N.s/m²)*	2.0e-3	-
E (N/m^2)	-	∞ / 3000.0
ν	-	0.3

Table 1: Geometrical and material properties of the fluid and solid domains.

3.1 Solid background integration mesh

As explained in Liu (2003) and Dolbow et al. (1998), the Element Free Galerkin Method (IEFGM is an extension of EFG) requires a background mesh for the integration of system matrices derived from the weak form of the governing equations. In this work, we considered only one solid geometry, a disk. To mesh this geometry we used an algorithm that produced a Delaunay triangulation of a set of points. Some modifications to the original code were made so that it would respect the boundaries of the domain throughout the triangulation process. The Eulerian and Lagrangian meshes used in the simulations are shown in Figure 3.1.

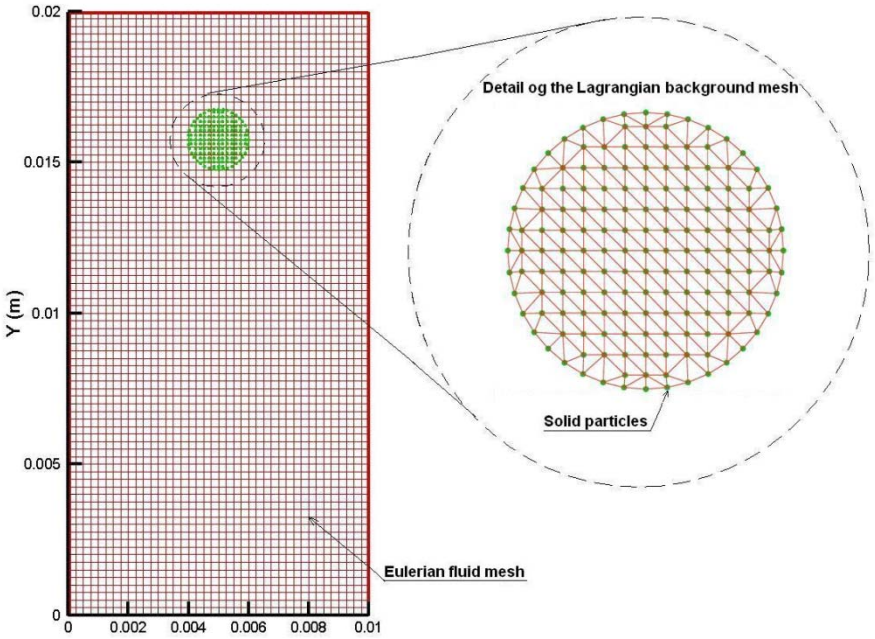

Fig. 3.1: Detail of the Lagrangian background mesh for the solid disk on top of the Eulerian fluid mesh.

3.2 Rigid disk falling in a viscous fluid

As first example, we studied the case of a rigid disk falling in an incompressible viscous fluid due to gravity. The properties of the solid material and the disk geometrical dimensions are specified in Table 1. To solve this problem we should set the solid material's Young modulus (E) to be as high as possible. However, as mentioned in Li et al. (2004), we verified that setting a high Young modulus would require a very small time step, which is not computationally efficient. Therefore we approached the problem as done in Li et al. (2004). We calculated the fluid velocity profile (using Eq. 10 and Eq. 11) setting E to the highest possible value that allowed us to work with a computationally efficient time step. Afterwards, we computed and assigned to all the solid particles, the average solid velocity.

$$\overline{\boldsymbol{v}^s} = \frac{\sum_{j=1}^{npl} \boldsymbol{v}^s{}_j}{n_{pl}} \tag{24}$$

In Eq. 24, the summation considers all the solid particles npL.

Fig. 3.2 shows the simulation results for this case. As soon as the solid disk starts to fall, vortices start to form around the solid-fluid interface. The terminal velocity of the solid is 0.118 m/s (≅12cm/s) calculated at time t = 0.125s. The position of the rigid disk and the velocity field at different time steps are shown in Fig. 3.2, with a detailed close-up in Fig. 3.2(e).

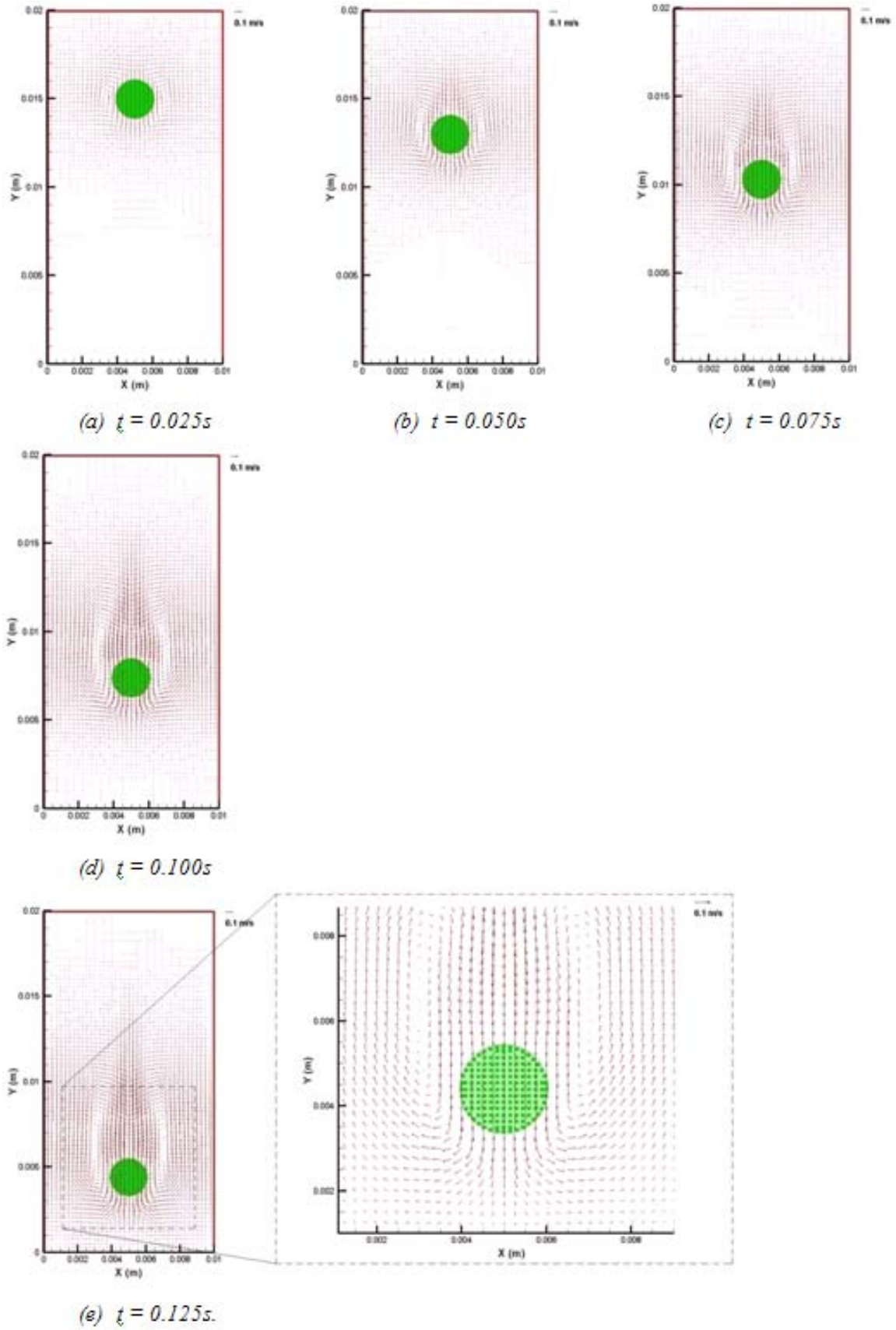

Fig. 3.2: Terminal Eulerian velocity field in the case of a rigid disk falling in a viscous fluid. A detail of the velocity field in the vicinity of the solid-fluid interface is shown in (e).

3.2.1 Comparison with analytical solution

The movement of a rigid solid body falling in a viscous fluid by the action of gravity is governed by a balance between the weight of the body, the buoyancy force, the drag of the fluid and the inertial force. Therefore, the force balance in the direction of gravity can be written as:

$$\rho^s Vol^s g - F_D - \rho^f Vol^s g = \rho^s Vol^s \frac{dv^s}{dt} \tag{25}$$

Considering the volume of a circular cylinder of length L and the expression for the drag force from White (1986), we can write:

$$Vol^s = \pi r^2 L$$
$$F_D = C_D(\tfrac{1}{2})2rL\rho^f (v^s)^2 \tag{26}$$

The drag coefficient C_D, is a function of the Reynolds number:

$$C_D(Re_d) = C_D\left(\frac{\rho^f v^s d}{\mu}\right) \tag{27}$$

Even though Eq. 27 shows a dependency of the drag coefficient upon the velocity, in this work we considered a constant value of C_D. This is justified because the disk reaches quickly the terminal velocity and in the range of Reynolds analyzed (~1000), the drag coefficient is fairly constant White (1986).

Introducing Eq. 26 into Eq. 25, we obtain:

$$\frac{dv^s}{dt} = \tilde{g} - C_D\left(\frac{\rho^f}{\rho^s \pi r}\right) v^2 \tag{28}$$

where

$$\tilde{g} \stackrel{\text{def}}{=} \frac{\rho^f - \rho^s}{\rho^s} g$$

Considering a constant drag coefficient, the solution of the first order differential equation expressed by Eq. 27 is:

$$v^s = v_t Tanh\left(\sqrt{C_D \frac{\rho^f \tilde{g}}{\rho^s \pi r}}\, t\right)$$
$$v_t \stackrel{\text{def}}{=} 2\tilde{g}\tau$$
$$\tau \stackrel{\text{def}}{=} \sqrt{\frac{\rho^s \pi r}{4\rho^f \tilde{g} C_D}} \tag{29}$$

Eq. 29 expresses the velocity of a rigid circular cylinder falling by gravity inside a viscous fluid domain considering a constant drag coefficient. The velocity v_t is the terminal velocity of the solid and τ is the characteristic time during which the body reaches 46% of v_t. The drag coefficient C_D for a circular cylinder with $L/d=\infty$ can be obtained from White (1986) as a function of the Reynolds number. In the numerical solution, the velocity of the solid domain in the direction of gravity ranges from v^s = 0.0114 m/s. (at time t=0.004s) and v^s = 0.11840m/s (at time t=0.125s). For these limits, we obtain the drag coefficients shown in Table 2.

Solid velocity v^s (m/s)	Re_d	C_D (White (1986))
0.0114	100	1.33
0.118	1038	1.0

Table 2: Reynolds numbers and drag coefficients for the limiting solid velocities in the numerical calculation of a rigid sphere falling in a viscous fluid.

Since the drag force (Eq. 26) is directly proportional to the square of the solid velocity, the higher the velocity, the larger the drag force. Therefore the value of the drag coefficient for large Re_d has more influence over the solid velocity history than that for smaller Re_d. For this reason, and since Eq. 29 is valid for a constant C_D, we chose C_D=1.0 to be representative of the drag coefficient throughout the simulation.

In Fig. 3.3, a comparison between the solid velocity histories obtained using the theoretical approach given by Eq. 29 and the IEFGM method is presented. We considered three different values of the Young modulus for the solid domain (E=3000N/m^2, E=30000N/m^2 and E=100000N/m^2). It can be seen that the IEFGM velocity is always higher than the theoretical velocity and, as the Young Modulus increases, the numerical solution approaches the analytical solution. The reason for this lies in the main approximation considered to solve the fall of a rigid solid body. As previously mentioned, this approximation consists in solving the velocity field considering a deformable body (finite Young modulus) and then assigning, at each time step, the average solid velocity to each solid particle. Even though this approximation allows the solid to keep its shape throughout the simulation, within each time step the algorithm is solving the fall of a deformable body. This flexibility of the disk decreases the viscous drag force of the fluid (the frontal area of the disk is kept constant throughout the simulation), hence increasing the magnitude of the solid's velocity. This gives, at each time step, a larger disk velocity compared to the theoretical result.

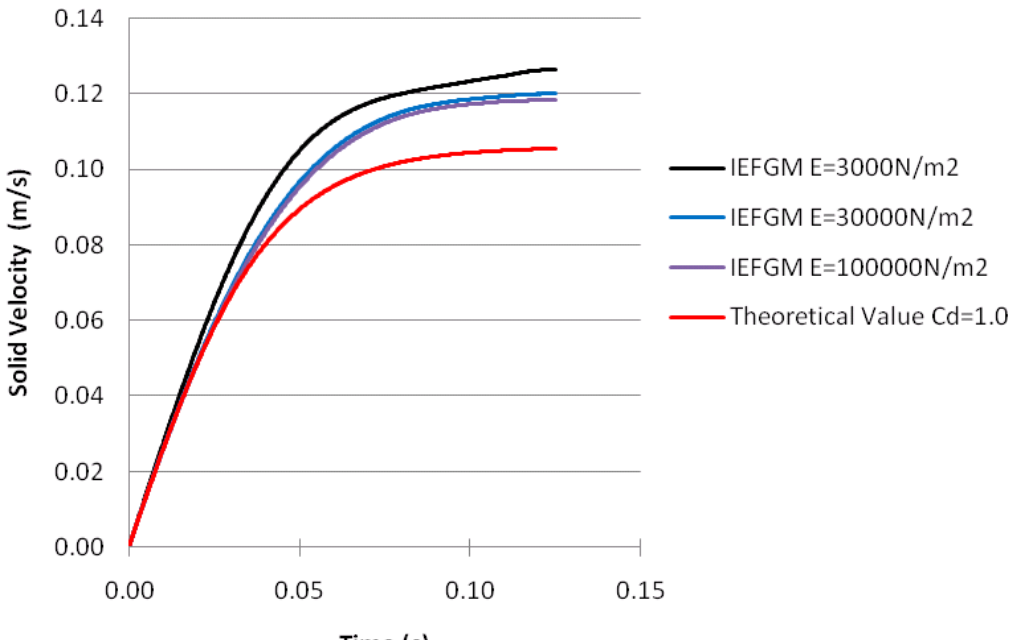

Fig. 3.3: Comparison between the velocity histories of a rigid solid disk falling in a viscous fluid obtained using the theoretical approach of Eq. 29 and IEFGM. A drag coefficient equal to 1.0 was used in Eq. 29 and three different values of Young modulus were considered in the rigid-body IEFGM calculation.

The numerical and theoretical terminal velocities are 0.11840m/s and 0.10542m/s respectively. The maximum difference between the theoretical and numerical results considering a Young modulus E=100000N/m^2 is approximately 14% (at t=0.125s).

3.3 Soft disk falling in a viscous fluid

In this section we present the case of a soft disk falling in the same Eulerian fluid. The geometrical and material properties of both domains are presented in Table 1.

The fluid velocity profile and the soft disk deformation process are shown in Fig. 3.4 at different times. It can be seen that the deformation is symmetric as expected. The last figure of the sequence shows an enlarged view of the deformation of the disk and the velocity field around it. We can see in this sequence that the lower part of the disk becomes wider throughout the simulation. The reason for this lies in the fact that we considered a large value of solid density (from Table 1 ρ^s = 12000K/m^3,in comparison to the value used by Zhang and Gay in Zhang et al. (2007), ρ^s = 3000K/m^3), hence the weight of the solid largely overcomes its rigidity making the front edge flatten as it falls through the fluid.

It is important to mention that since the interaction force f_i^{FSI} is included in an explicit manner into Eq. 10, the use of a large value of the Young modulus requires a rather small time step. For the range of Young modulus considered in this work, (3000 – 100000 N/m^2) the time step required for convergence was in the order of 10^{-4} s. This fact affects the computational efficiency of the method, and an implicit formulation would be required to overcome this shortcoming. The time step size is also affected by the velocity of the solid and the Eulerian mesh size. Note however, that the IEFG method handles rather well solids with very large deformation and with Young modulus considerably larger than simulated in previous works (E=1000 in Zhang et al. (2007)).

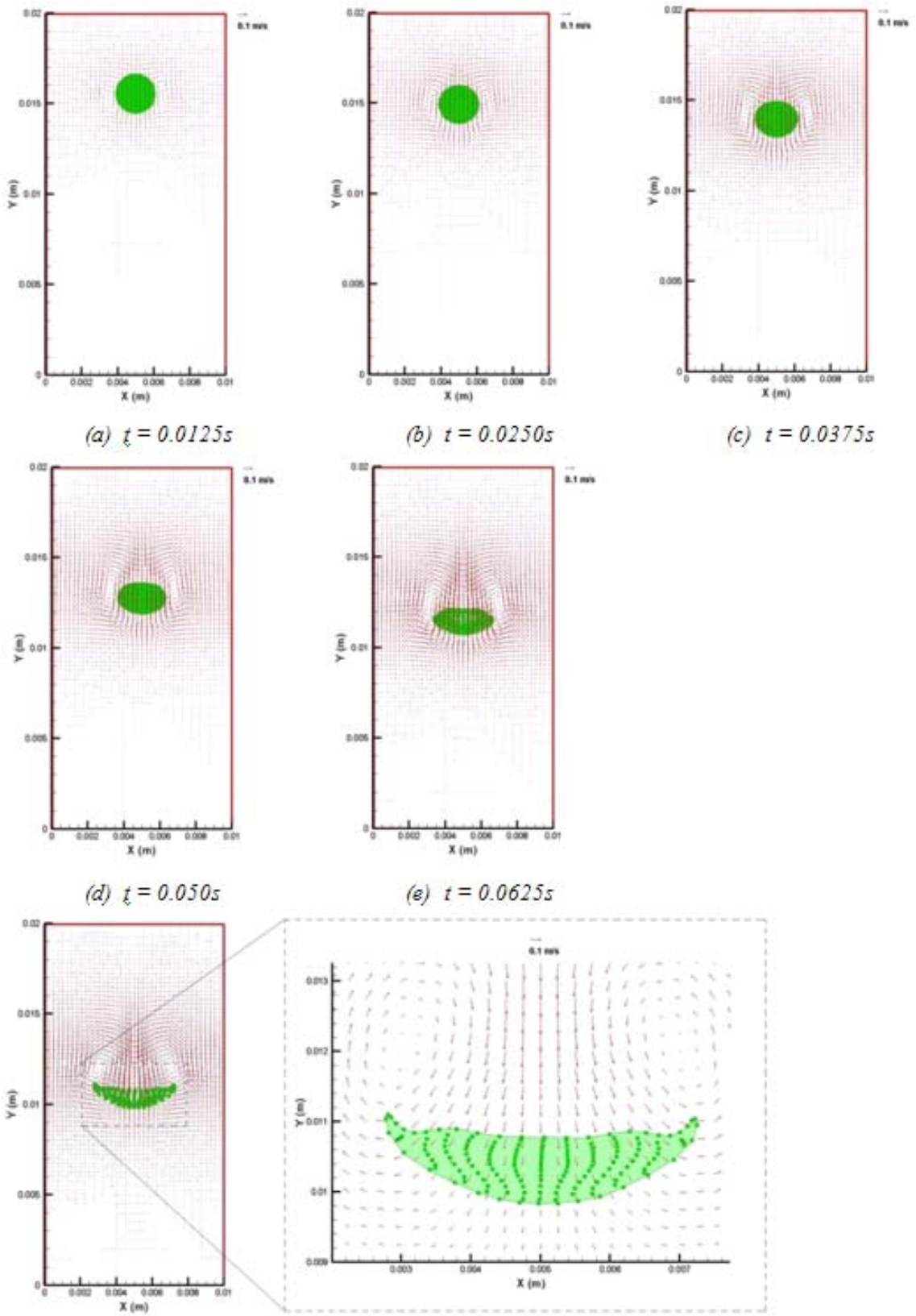

Fig. 3.4: Eulerian velocity field and Lagrangian solid at different times in the case of a soft disk falling in a viscous fluid. A detail of the final shape of the disk at t=0.0750s and the fluid velocity field in the vicinity of the solid-fluid interface is shown in (f).

3.3.1 Comparison between rigid and soft disks

It is interesting to compare the positions of the rigid and soft disks at time t = 0.0750s (refer to Figures 3.2 and 3.4). In Fig 3.5, we show in detail such comparison. We can see that the rigid disk falls faster than its soft counterpart. The explanation for this can be found in the definition of the drag force given in Eq. 26. As we can see in this equation, the drag force is directly proportional to the frontal area (which is the area as seen from the fluid stream). In this example, the frontal area is given by:

$$A = dL$$

where L is the dimension in the z-direction (perpendicular to the page).

As we can see in Fig. 3.5, the characteristic lengths of the rigid disk and the soft disk, at time t = 0.0075s, are d=0.00200m and D=0.00446m respectively. The resulting frontal area of the deformed geometry is then 2.23 times bigger than that of the rigid circular geometry. This increase in the frontal area as the solid deforms, augments the drag force diminishing, in consequence, the velocity of the soft disk.

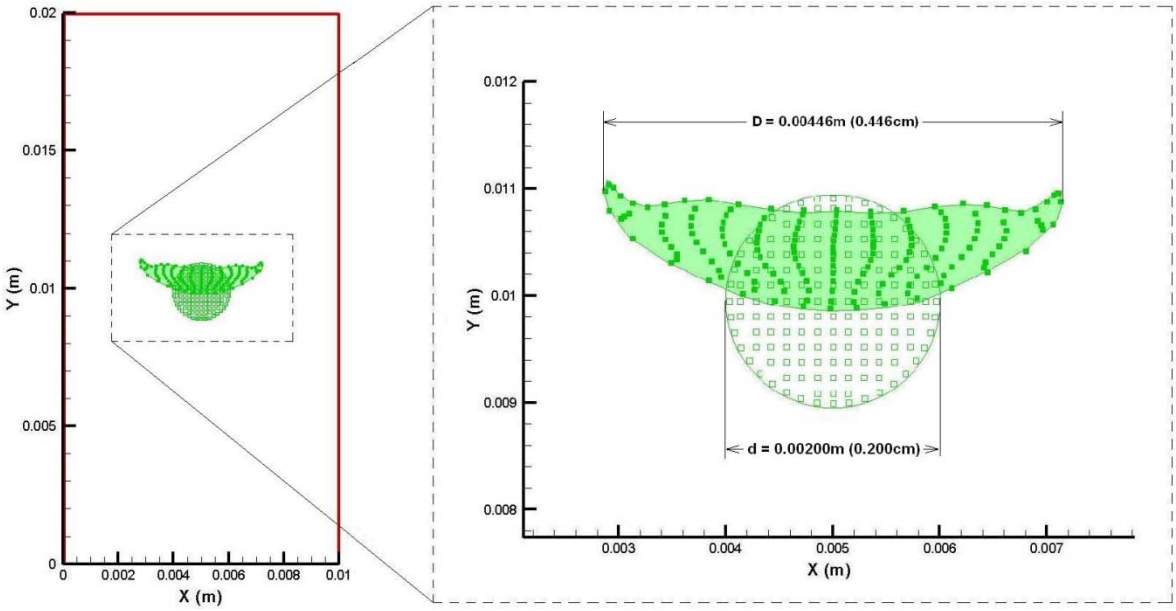

Fig. 3.5: Comparison between the solid and rigid disk's positions at t=0.0750s. The increase in the drag force due to the increase in the frontal area (area as seen from the fluid stream) of the soft disk reduces its velocity. Since the fluid velocity fields for both cases being compared are different, no information regarding the fluid velocity is shown in this figure.

A comparison between the velocity histories obtained for a rigid disk using theoretical results from Eq. 29 with C_D = 1.0, a rigid disk using IEFGM with a Young modulus E = 3000N/m^2, and a soft disk using IEFGM with a Young modulus E = 3000 is presented in Fig. 3.6.

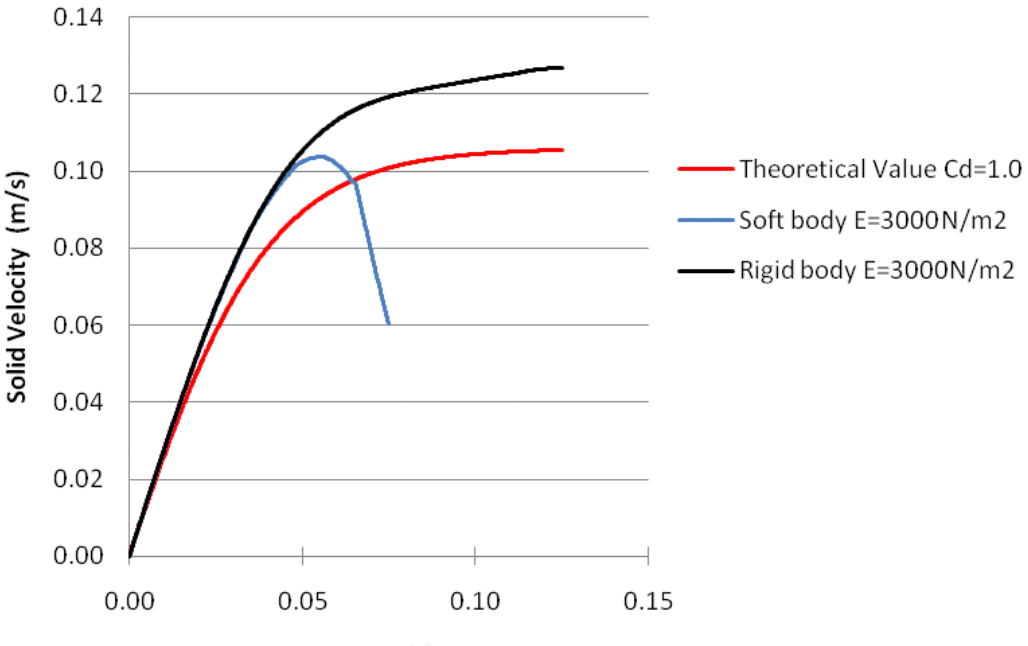

Fig. 3.6: Comparison between the velocity histories obtained for rigid and soft disks. The theoretical solution for a rigid disk was obtained using Eq. 29 with C_D = 1.0. The IEFGM solution for a rigid disk was obtained considering E = 3000N/m^2 and the rigid body approximation explained in Section 3.2. The IEFGM solution for a soft disk was obtained considering E = 3000N/m^2.

We can see that when the effect of the increasing frontal area starts to significantly affect the drag force, the velocity of the soft disk decreases and eventually becomes smaller than the velocity of the rigid disk. The separation between the numerical solutions for the rigid and soft disks was produced at t = 0.041s which corresponds to a velocity in the direction of gravity v^s = 0.093m/s.

4 CONCLUSIONS

A new numerical approach (Immersed Element-Free Galerkin) was developed for the solution of fluid-structure interaction problems. The method was applied to simulate the free fall of rigid and deformable solids in a viscous fluid. Good performance of the method was obtained when comparing simulated results with analytical solutions. The use of a meshfree particle method (Element-Free Galerkin) to model the solid domain and the solid-fluid coupling through MLS interpolants gives the proposed approach a potential advantage for simulating FSI problems with highly deformable solids. Although the method handles rather well solids with Young modulus considerably larger than those simulated in previous works, the explicit treatment of the FSI force in the momentum equations introduces a limitation in the time step size when simulating rigid bodies or solids with realistic values of the elastic coefficients.

5 ACKNOWLEDGMENTS

This work was partly funded by the National Science Foundation through Grant Number CTS-0553570. The authors gratefully appreciate the financial support provided by the Center for Advanced Vehicular Systems (CAVS) at Mississippi State University.

REFERENCES

Atluri, S., Zhu, T., A new Meshless Local Petrov Galerkin (MLPG) approach in computational mechanics. *Computational Mechanics*, Vol. 22, pp 117-127, 2000.

Attaway, S. W., Heinstein, M.W., and Swegle, J.W., Coupling of smooth particle hydrodynamics with the finite element method. *Nuclear Engineering and Design*, Vol. 150, pp. 199-205, 1994.

Belytschko T., Krongauz, Y., Organ, D., Fleming, M., Krysl, P., Meshless Methods: An overview and recent developments. *Computer Methods in Applied Mechanics and Engineering*, Vol. 139, pp. 3-47, 1996.

Belytschko, T., Lu, Y.Y., and Gu, L., Element-free Galerkin methods. *International Journal for Numerical Methods in Engineering*, Vol. 37, pp. 229-256, 1994.

Belytschko, T., Xiao, S., Stability Analysis of Particle Methods with Corrected Derivatives. *Computers & Mathematics with Applications*, Vol. 43, Issues 3-5, pp. 329-350, 2002.

Benz, W., Smooth particle hydrodynamics: a review. In J.R. Buchler, editor. *The Numerical Modeling of Nonlinear Stellar Pulsatations*, pp. 269-288. Kluwer Academic Publishers, 1990.

Dilts, G. A., Moving –least squares-particle hydrodynamics I, consistency and stability. *International Journal for Numerical Methods in Engineering*, Vol. 4, pp. 1115-1155, 1999.

Dolbow, J. and Belytschko, T., An Introduction to Programming the Meshless Element Free Galerking Method. *Archives of Computational Methods in Engineering - State of the art reviews* - , Vol. 5, 3, pp. 207-241, 1998.

Felicelli, S.D., Heinrichi, J.C., and Poirier, D.R.: Numerical models for dendritic solidification of binary alloys. *Num. Heat Trans. B*, vol.23, pp.461-481, 1993.

Gingold, R.A. and Monaghan, J.J., Smoothed particle hydrodynamics: theory and application to non-spherical stars. *Monthly Notices Royal Astronomical Society*, Vol. 181, pp. 375-389, 1977.

Johnson, G.R., Linking of Lagrangian particle methods to standard finite element methods for high velocity impact computations. *Nuclear Engineering and Design*, Vol. 150, pp. 265-274, 1994.

Krongauz, Y., Belytschko, T., Consistent pseudo derivatives in meshless methods. *Computer Methods in Applied Mechanics and Engineering*, Vol 146, pp. 371-386, 1997.

Lancaster, P. and Salkauskas, K., Surfaces Generated by Moving Least Squares Methods. *Mathematics of Computation*, Vol. 37, Number 155, pp. 141-158, July 1981.

Levin, D., The approximation power of Moving Least Squares. *Mathematics of Computation*, Vol. 67, Number 224, pp. 1517-1531, 1998.

Li, S., Liu, W.K., Meshfree Particle Methods. *Springer-Verlag* Berlin Heidelberg, 2004.

Libersky, L.D., Petschek, A.G, Carney, T.C., Hipp, J.R., and Allahdadi, F.A., High Strain Lagrangian Hydrodynamics. *Journal of Computational Physics,* Vol. 109, pp. 67-75, 1993.

Libersky, L.D., Petschek, A.G., Smooth particle hydrodynamics with strength of materials. Advances in the Free Lagrange Method. *Lecture Notes in Physics*, Vol. 395, pp. 248-257, 1990.

Liu, G.R., Mesh Free Methods – Moving beyond the Finite Element Method. *CRC Press* – Boca Raton, Florida, USA, 2003.

Liu, W. K., Adee, J., Jun, S., Reproducing kernel particle methods for elastic and plastic problems. In: Benson D.J., Asaro R.A.(eds.). *Advanced Computational Methods for Material Modeling*, AMD 180 and PVP 33, ASME, pp.175-190, 1993.

Liu, W.K., Jun, S., Li, S., Adee, J., Belytschko, T., Reproducing kernel particle methods for structural dynamics. *International Journal for Numerical Methods in Engineering*, Vol 38,

pp. 1655-1679, 1995.

Lucy, L.B., A numerical approach to the testing of fusion process. *Astronomical Journal*, Vol. 88, pp. 1013-1024, 1977.

Monaghan J. J., Why particle methods work. *SIAM Journal on Scientific and Statistical Computing*, Vol 3(4), pp. 422-433, 1982.

Randles, P. W., Libersky, L. D., Petschek, A. G., On neighbors, derivatives, and viscosity in particle codes. In: *Proceedings of ECCM Conference*, Munich, Germany, 31 August–3 September 1999.

Randles, P. W., Libersky, L. D., Smoothed particle hydrodynamics: Some recent improvements and applications. *Computer Methods in Applied Mechanics and Engineering*, Vol. 139, pp375-408, 1996.

Swegle, J. W., Attaway, S. W., Heinstein, M. W., Mello, F. J., and Hicks, D. L., An analysis of smooth particle hydrodynamics. *Sandia Report* SAND93-2513, 1994.

Vignjevic, R., Campbell, J., Libersky, L. A., Treatment of Zero Energy Modes in the Smoothed Particle Hydrodynamics Method. *Computer Methods in Applied Mechanics and Engineering*, Vol. 184/1, pp 67-85, 2000.

Wen, Y., Hicks, D. L. and Swegle, J. W., Stabilising SPH with conservative smoothing. *Sandia Report* SAND94-1932, 1994.

White. F.M., Fluid Mechanics. *McGraw-Hill Book Company*, 2nd Ed., 1986.

Zhang, L., Gerstenberg, A., Wang, X., and Liu, W.K., Immersed Finite Element Method. *Comput. Methods Appl. Mech Engrg*. 193, pp. 2051-2067, 2004.

Zhang, L.T. and Gay, M., Immersed Finite Element Method for fluid-structure interaction. *Journal of Fluids and Structures*, Vol. 23, Issue 6, pp. 836-857, August 2007.